Experimentally Determined Material Parameters for Temperature Prediction of an Automobile Tire using Finite Element Analysis

W.B. van Blommestein[a], G. Venter[b], M.P. Venter[c]

Received 16 January 2019, in revised form 1 July 2019 and accepted 23 July 2019

Abstract: The material parameters of an automotive truck tire were experimentally determined and validated for use in a thermal finite element analysis to determine the temperature distribution in the tire due to different operating conditions. Uni-axial tensile tests were performed on tire samples. The force displacement response of each was used to determine material properties by means of direct curve-fitting and iterative numerical procedures. Equivalent finite element simulation models were used to validate the properties. Hysteresis behaviour of the rubber regions were identified by dynamic mechanical analysis. Material definitions were incorporated into a finite element model to predict the steady-state heat generation and temperature distribution within a tire due to hysteresis. Experimental rolling tire temperature measurements were taken on a test bench. A comparison of the results with those obtained from the equivalent thermal models was used to validate the numerical models.

Additional keywords: Temperature prediction, Hysteresis heating, Uni-axial tensile test, DMA .

Nomenclature

Roman

C	Model coefficients
H_c	Film coefficient
I	Strain invariants
L	Length [m]
U	Strain-energy density [J/m^3]
V	Velocity [m/s]
W	Mooney Rivlin strain-energy [J/m^3]

Greek

λ	Stretch ratio

Subscripts

10	First order Mooney Rivlin coefficient
01	Second order Mooney Rivlin coefficient
11	Third order Mooney Rivlin coefficient
1	First order strain invariant / stretch ratio
2	Second order strain invariant / stretch ratio
3	Third order strain invariant / stretch ratio
i	Initial/increment

1 Introduction

Thermo-oxidation is the irreversible chemical and mechanical decomposition of a material due to heat, resulting in the release of volatile gases [1]. It may occur within the rubber regions of a pneumatic automotive tire during normal use. In such an event the pressure increases within the tire cavity, as long as the temperature continues to rise, leading to an increased oxidation rate. A similar process called pyrolysis could occur in the absence of oxygen [1], such as the case when the tire is inflated with nitrogen. The temperature response of a material undergoing pyrolysis is greatly affected by the heating rate of the material [2].

When a material that exhibits hysteresis, such as rubber, undergoes cyclic loading a fraction of the required elastic deformation energy (elastic strain-energy) is absorbed and converted to heat (loss strain-energy). This is due to a phase lag that exists between the strain and stress response curves of such a material [3,4], that can be defined by its hysteresis coefficient value. Hysteresis is a major source of energy loss within a tire [5][6], resulting in unavoidable internal heat generation during normal use. The dynamic mechanical properties of rubber materials, related to the materials hysteresis response, have been shown to be subject to fatigue induced change, associated with endurance limitations of the material [7,8].

Several overheating cycles will cumulatively degrade the tire structure until failure occurs in the form of a blow-out, during which the weakened structure would give way under the increased inflation pressure. A more severe mode of failure would occur if the gas temperature and pressure were to exceed the auto-ignition point of the inflation medium. The mixture would self-ignite, resulting in a violent explosion. The ability to accurately predict tire operating temperatures under a variety of loading conditions would benefit the automotive and mining industry, due to the

a. Department of Mechanical Engineering, Stellenbosch University, South Africa. E-mail: wilburvanblommestein@gmail.com
b. SAIMechE Member. Department of Mechanical Engineering, Stellenbosch University, South Africa. E-mail: gventer@sun.ac.za.
c. SAIMechE Member. Department of Mechanical Engineering, Stellenbosch University, South Africa. E-mail: mpventer@sun.ac.za.

potential loss of life and machinery associated with the explosion of tires.

A finite element (FE) modelling procedure was created to simulate the inflation, loading and steady state rolling behaviour of a steel belted radial truck tire as three individual models. The models made use of the non-linear two- and three-term Mooney Rivlin strain-energy based material definitions for its rubber components, while the reinforcement steel and cord rebar components were modelled as linear isotropic materials. Material parameters of the tire components were determined and validated experimentally, followed by their incorporation into the simulation models, as advised by Kovac and Krmela [9]. Elastic strain-energy density resulting from deformation of the elastomer material during a single rotation was used to estimate the magnitude of heat generation due to hysteresis within a cross sectional set of elements. This information was then passed on to an axisymmetric thermal analysis of the tire to obtain a prediction of the tire temperature distributions [10]. Simulation results were finally compared to experimental results obtained from an experimental rolling road tire test bench. A detailed discussion of the modelling procedure is provided in section 2.

This paper presents a hysteresis based non-linear finite element thermal analysis procedure to predict the steady state rolling temperature distributions in an automotive tire using experimentally determined material parameters [10].

2 Numerical Simulation of the Tire

The modelling procedure, created within MSC's non-linear finite element package Marc, begins with an axisymmetric inflation analysis, as illustrated in figure 1, with the purpose of obtaining the inflated tire profile. Air was used as the working fluid, inflating the structure gradually by means of an inflation (pressure) control boundary condition, resulting in the tire mounting onto the bead seat of the rim. A flexible cavity surface element ensured an airtight seal during inflation. The model consisted of 801 elements and 953 nodes, with the rim being represented by a smooth analytical boundary. The modelling of different rubber and reinforcement compounds comprising the structure of the tire was carefully considered, consistent with numerical tire modelling completed by Kovac and Krmela [9], Ghosh [6], Ghoreishy [11], Korunović [12,13], Marais [14], Hölscher [15] and Yang [16].

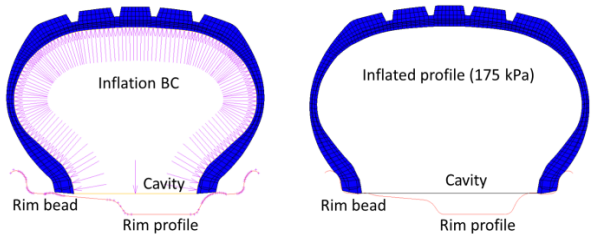

Figure 1: Axisymetric inflation simulation model, using an inflation controlled boundary condition and flexible cavity surface element (left). Inflated profile shape for 175 kPa on the right.

The inflated tire profile was then used as an initial condition within a 3-D load controlled analysis of the tire, as illustrated in figure 2. Its purpose was to identify the radial displacement magnitude of the tire, due to load application for a constant inflation pressure, relative to a cylindrical rolling road (drum) surface. Use of combined axisymmetric and full 3D models greatly reduces on the overall modelling cost requirements, consistent with simulations done by Korunović [12,13]. The geometry of the components matched those of an equivalent rolling road tire test bench, as discussed in section 4, which was used to validate the structural and thermal models. The 3-D model comprised of 57 672 elements and 67 609 nodes in total.

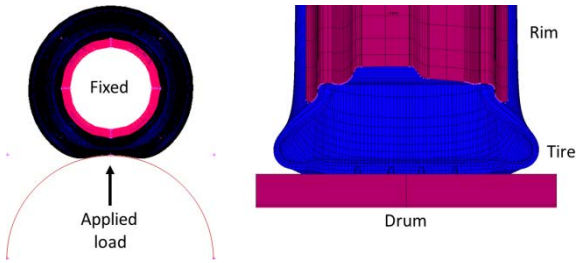

Figure 2: Loading analysis model, illustrating deformation for an applied load of 700 kg and inflation pressure of 100 kPa. Full side-view of the model provided on the left, with a cross-sectional view of the deformed (loaded) tire profile on the right.

The resulting displacement under load was then used as a displacement controlled boundary condition in the proceeding dynamic rolling analysis. This was to reduce the models computational requirements and total run time. The dynamic rolling analysis is a variation of the loading analysis, during which the wheel was rotated relative to the rolling drum surface at a constant velocity. Elastic strain-energy density (J/m^3) was then extracted from a cross sectional region of elements during a single rotation relative to the drum surface. The strain-energy density relates to the magnitude of energy that is required to elastically deform an element [17,5,18,4]. The total strain-energy density for each element node was calculated as the sum of increasing differences over the deformation increment range, with reference to equation 1 and figure 3. This process accounts only for strains produced within each cross sectional element due to a positive change in deformation energy [17].

$$TotalU_{SED} = \sum_{i=1}^{n} \Delta U_i \quad (1)$$

For each increment, the elemental equivalent strain-energy density was taken as the average of its nodal values. Total strain-energy density for each element was in turn equal to its sum over the entire deformation period, being equal to approximately one quarter of a rotation. The heat generated within each element due to hysteresis was obtained from the product of the total strain, the materials hysteresis coefficient and the particular rotational frequency [18,5]. Using a Python script, the heat generated within each element was calculated and incorporated into a final axisymmetric thermal analysis, as shown in figure 4.

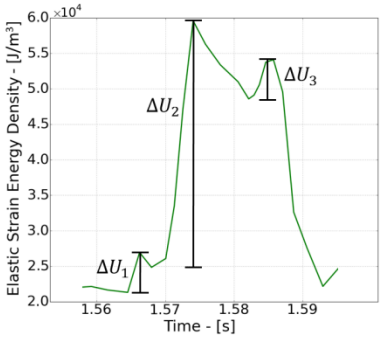

Figure 3: Nodal elastic strain-energy density increase during rotational deformation.

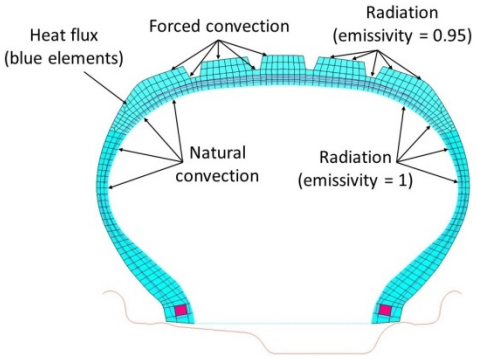

Figure 4: Thermal analysis boundary conditions.

Forced convection was applied to the external sidewall and tread surfaces as an edge film boundary, simulating the influence of air flow past the tire. The film coefficient (H_c) was calculated by equation. 2, as originally established by Browne and Wicklife [21], as a function of the forward wheel velocity (v) in m/s. This method of convection heat transfer was reported to have a dominating effect relative to the outside environment of a vehicle tire during rotation, with additional validations made by Ebbot *et al.* [22] and Assaad *et al.* [23]

$$H_c = 5.9 + 3.7v \quad (2)$$

A natural convection boundary condition was placed between the internal cavity surface and cavity air, assuming the relative cavity air velocity to be negligible. Ambient temperature magnitudes for both film boundaries were set equal to values measured during testing. Radiation effects were also included, with emissivity set to 0.95 for all external rubber surfaces [3], while the cavity was specified with a value of 1 [24]. Successful execution of the thermal analysis simulation resulted in a cross-sectional prediction of the heat distribution within the tire for a given radial load, inflation pressure and forward velocity.

3 Characterisation of Material Models

Tensile tests were performed on samples obtained from a 215/70R15 Maxtrek SU-830 steel-belted radial tubeless truck tire. Sample selection was based on the findings of cross-sectional durometer hardness measurements, computed tomography (CT) scans and an examination of the actual tire, as to obtain samples for testing that were representative of the modelled tire. The selection of samples and development of the 'direct experimental data fit' (refer section 3.1) and 'iterative methods' (refer section 3.2) for identification of material parameters, was an iteratively developed approach.

Owing to the physical size constraints of the tire, it was not possible to obtain samples conforming to the specific dimensional requirements of available ASTM standards. As such, samples were selected based on the aforementioned physical limitations (material availability, including directionality and internal layup) of the tire, while adhering to specified strain rates. Figure 5 provides an illustration of the major tire regions, as identified during the analysis of the tire structure.

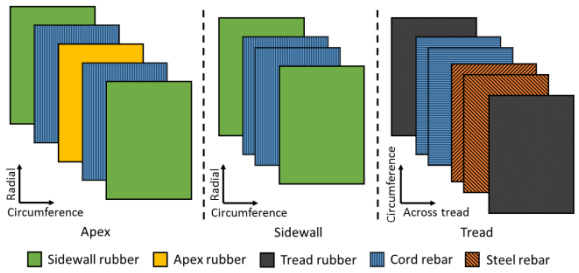

Figure 5: Illustration of tire structural regions.

Tests were conducted using a MTS criterion uni-axial test bench and LaVision stereoscopic DIC system. A test bench load cell measured tensile reaction force, while the DIC captured sample strain response. Stress-strain response curves were then used in a series of direct material curve-fitting and iterative numerical procedures to identify the various individual tire material properties. Similar test methodologies for obtaining data suitable for establishing material model coefficients have been reported by Gent [19], Ghosh [6], Yang [16], and Marais [14].

3.1 Direct experimental data fit

Properties were established directly from tensile test data for samples comprising of a single material, as per the previously defined regions (section 3). Three-term Mooney Rivlin constitutive models (equations 3 to 7) were used to simulate the tread and sidewall rubber regions (figure 5). Mooney Rivlin models are the most widely used strain-energy based functions [19,15,20] to simulate the non-linear response of elastomer (rubber) compounds in FEA, including automotive tire model applications. The two term model shows good agreement with tensile test data for strains of up to 100%, while the three-term model accounts for a non-constant shear modulus [19]. Furthermore, they easily provide strain energy data, resulting from a given material deformation, used to determine (simulate) the rate of heat generation owing to hysteresis.

Model coefficients (C_{10}, C_{01} and C_{11}) were obtained by means of an experimental data fit tool within the MSC. Marc pre-processor software Mentat. It executed a time-independent fit of the material model equation onto a given stress-strain data curve, while automatically minimising the least squares error relative to the curve by adjustment of the coefficient values.

The Mooney Rivlin strain-energy function W (J/m^3) is an invariant-based treatment of rubber that effectively models strain-energy response due to deformation, based on experimentally observed sample response data. The strain invariants (I_1, I_2 and I_3), which are based on the principal strain magnitudes, are functions of the stretch ratios (λ_1, λ_2 and λ_3) of the material with respect to an initial length (L_i). Tang *et al.* [5] and Lin and Hwang [18] successfully simulated the thermal response of a tire when using it to represent its elastomer components. In addition, for incompressibility, I_3 is equal to 1 [25]. A further simplification on the Mooney model, known as the Yeho model, in which the I_2 term is substituted for I_1, which greatly simplifies the problem of determining coefficients [19], was successfully used by Ghosh [6] and Yang [16].

$$W = C_{10}(I_1 - 3) + C_{01}(I_2 - 3) + C_{11}(I_1 - 3)(I_2 - 3) \quad (3)$$

$$I_1 = \lambda_1^2 + \lambda_2^2 + \lambda_3^2 \quad (4)$$

$$I_2 = \lambda_1^2\lambda_2^2 + \lambda_2^2\lambda_3^2 + \lambda_3^2\lambda_1^2 \quad (5)$$

$$I_3 = \lambda_1^2\lambda_2^2\lambda_3^2 \quad (6)$$

$$\lambda_i = \frac{L_i + dL_i}{L_i} \quad (7)$$

The Mooney Rivlin model provided an accurate representation of the sidewall and tread rubber samples non-linear response curves. Figures 6 and 7 illustrate the resulting fits for the sidewall- and tread rubber regions respectively. The root mean squared (RMS) errors between the numerical and experimental curves, along with their respective coefficient values are provided in table 1.

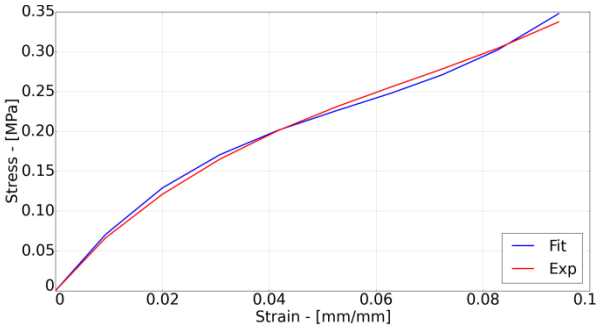

Figure 6: Sidewall rubber Mooney Rivlin 3-term data fit.

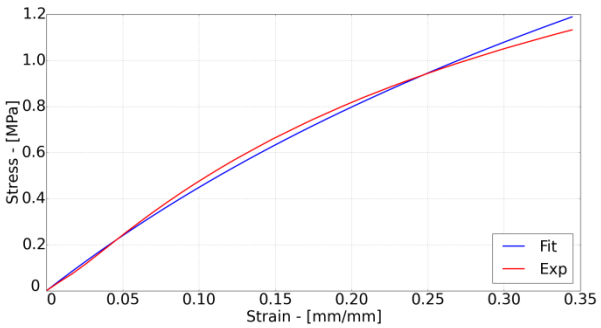

Figure 7: Tread rubber Mooney Rivlin 2-term data fit.

The obtained Mooney Rivlin material coefficient values were subject to a set of stability requirements [26]. Stability in this context referred to a positive increase in material strain resulting in a positive stress response. The material models cannot simulate a reduction in stress due to increased strain magnitudes. Criteria for both two- and three-term variants of the model [26], to which the coefficient values of table 1 conformed, can be viewed in equations 8 and 9 respectively.

Table 1: Mooney Rivlin material coefficients obtained from direct experimental curve fits.

	Sidewall	Tread
C_{10}	-1.87597e+007	440161
C_{01}	2.02023e+007	417869
C_{11}	2.07861e+007	-
Bulk moduli	1.44262e+010	8.5803e+009
RMS error	0.006	0.024

$$C_{10} + C_{01} \geq 0 \;\&\; C_{01} \geq 0 \quad (8)$$

$$C_{10} + C_{01} \geq 0 \;\&\; C_{11} \geq 0 \quad (9)$$

The inner tire tread region contained two adjacent layers of steel rebar, at positive and negative 30 degree angles relative to its circumference (figure 5). Each layer consisted of multiple parallel steel cables, with four wound steel wires making up each cable. Individually tested cable samples exhibited linear stress-strain responses, as shown in figure 8. Each cable was subsequently modelled as an isotropic material, utilising a rebar element definition [27] to represent the entire reinforcement structure. Material properties are provided in table 2, along with geometric parameters that were identified by means of a digital Vernier calliper and mechanical micrometer.

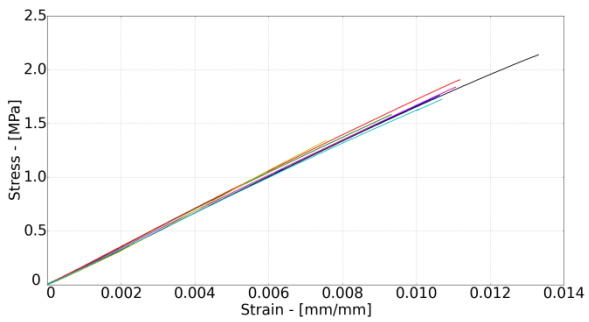

Figure 8: Stress-strain response curves of steel rebar samples.

Table 2: Steel rebar parameters and properties, with rebar area referring to the cross sectional area of an individual rebar unit. Unit spacing along the tire cross section equal to the set number of rebars per unit length.

Parameter	Value
Elastic modulus	170.4 GPa
Poissons ratio	0.3
Number of rebars per length	675/m
Rebar area	2.290e-007m^2

3.2 Iterative methods

The complex structure, geometry and materials composition of the test tire, as per figure 5, made it difficult to perform tensile tests on each material individually. This was the case for the apex rubber within the lower sidewall region and

http://dx.doi.org/10.17159/2309-8988/2019/v35a3

radial cord rebars within the tire sidewall. It was however possible to obtain combined material samples, from which these material parameters could be identified by means of an inverse iterative approach. Apex samples comprised of a central apex rubber region, with adjacent sidewall rubber strips on either side, while the cord rebar was encapsulated within a uniform strip of sidewall rubber. Apex samples were tested in the circumferential direction, wherein the radial cord rebar influence was negligible. With the sidewall rubber material coefficients already established, the stress-strain contribution of the unknown material could be identified as the difference between that of the combined and known-material responses.

Numerically equivalent tensile simulation models were created of both samples, using initial estimates for the unknown material in each case. A Python script employing a gradient based numerical optimisation tool (DOT), developed by Vanderplaats research and development [28], was then used to iteratively adjust (optimise) the material coefficient values. DOT is a multi-purpose software library employing well-established gradient based numerical optimisation methods to maximise or minimise an objective function of interest. It does so by adjusting a set of design variables subject to a selection of inequality and/or side constraints specified by a particular application. The objective function of interest, that was to be minimised, was that of the RMS error between the numerical and experimental combined material stress-strain response curves, with the design variables being the initially guessed material parameters. The optimisation procedure is illustrated in figure 9.

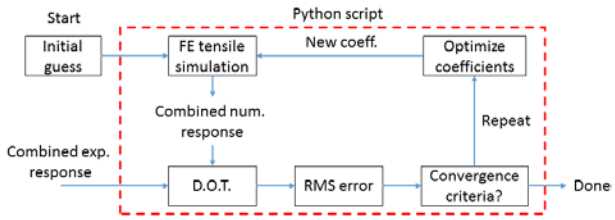

Figure 9: Iterative optimization loop used for the identification of the apex rubber and cord rebar material parameters.

The apex rubber was modelled by the three-term Mooney Rivlin model (equation 3), with figure 10 illustrating the final numerical (num) versus experimental (exp) force-strain response curves of the combined material tensile sample. Material coefficients, as well as the RMS error between the experimental and numerical response curves, can be viewed in table 3. The converged coefficient values conformed to the Mooney Rivlin stability criterion, as per equation 9.

Table 3: Initial and converged three-term Mooney Rivlin apex rubber coefficients.

Coefficient	Initial estimate	Converged value
C_{10}	-1.87597e+007	-1.07124e+008
C_{01}	2.02023e+007	1.16883e+008
C_{11}	2.07861e+007	1.04791e+008
RMS error	-	0.945

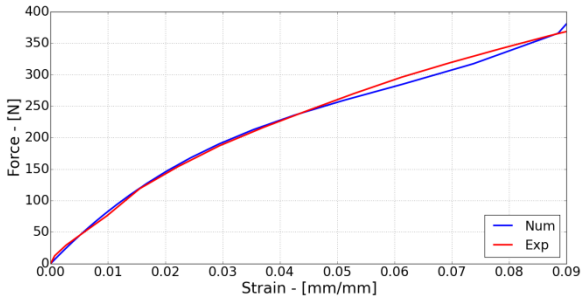

Figure 10: Combined material apex tensile sample results comparison, using material coefficients obtained from optimization procedure.

The radial cord rebar was modelled as an isotropic material, with final converged material properties and geometric parameters provided in table 4, wherein the 'number of rebar' and 'rebar area' refer to the modelled geometry. The rebar structure was modelled by using a rebar element formulation [27]. The numerical versus experimental sidewall radial combined material tensile response curves can be viewed in figure 11. The combined response refers to the contribution of both the rubber and cord rebar materials as a composite, as found in the tire sidewall.

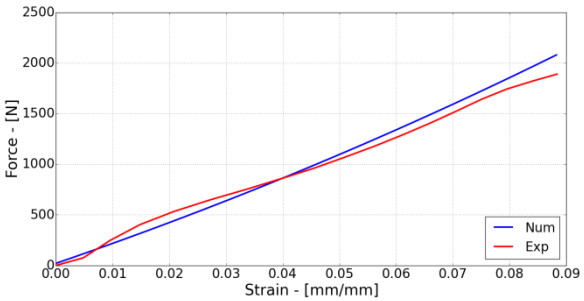

Figure 11: Combined material sidewall radial tensile test sample result comparison.

Table 4: Cord rebar parameters and properties, with rebar area referring to the cross sectional area of an individual rebar unit. Unit spacing along the tire cross section equal to the set number of rebars per unit length.

Parameter	Value
Elastic modulus	497 GPa
Poissons ratio	0.1
Number of rebars per length	1025/m
Rebar area	5.026e-007m^2

3.3 Numerical model material regions

Figure 12 provides a cross sectional illustration of the simulation model material region definitions, as identified during the experimental material characterisation procedure, with material parameters as per the direct experimental and iterative procedures.

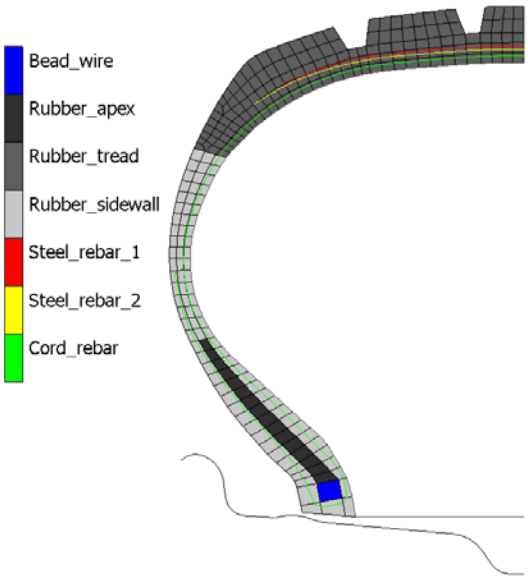

Figure 12: Illustration of the cross sectional numerical simulation model material regions.

3.4 Hysteresis coefficients

The thermal tire simulation models (section 2) required hysteresis coefficient values of each elastomer region for heat generation calculations. Dynamic mechanical analysis (DMA) measurements were conducted on rubber samples from the apex, sidewall and tread regions (figure 5). A dual cantilever beam testing procedure was used, measuring both storage and loss modulus respectively. Three excitation frequencies were evaluated, corresponding to forward wheel hub velocities of 20, 40 and 60 km/h, with final coefficient values provided in table 5. This was in contrast to a value of 0.1, advised by published literature sources [17,5,18].

Table 5: Hysteresis coefficient values used for numerical thermal simulation models, as identified through experimental DMA testing.

Excitation frequency	Apex	Tread	Sidewall
2.59 Hz (20 km/h)	0.25	0.17	0.35
5.18 Hz (40 km/h)	0.18	0.15	0.29
7.78 Hz (60 km/h)	0.16	0.16	0.31

4 Experimental Results and Comparison

An experimental rolling road tire test bench, as illustrated in figure 13, was used throughout the project for structural and thermal model validations. It consisted of an axial fan-driven wind tunnel, a 0.87 m diameter steel rolling drum and an electrically driven wheel hub. This allowed a test wheel to be driven at a constant velocity against the drum, as to simulate a continuous road surface, whilst simulating vehicle air flow by the fan unit. The cylinder was height-adjustable by means of a hydraulic jack, allowing it to exert a constant contact pressure onto the tire tread, using a load cell to measure the reaction force. A programmable logic controller (PLC) user interface was used to control and monitor the drive motor, axial fan unit, load-cell and various temperature and pressure sensors.

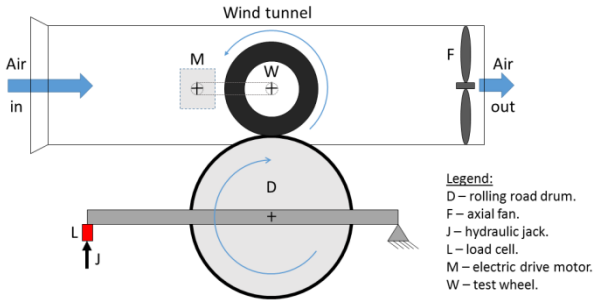

Figure 13: Illustration of experimental rolling road tire test bench.

Three infra-red Calex PyroCouple temperature sensors were used to measure the surface temperature of the internal cavity. Sensor locations and orientations were selected to provide readings of the central tread, shoulder and central sidewall regions respectively. Each sensor provided an area-averaged temperature reading of the surface region it illuminated, as illustrated in figure 14 (left). Corresponding numerical results were subsequently extracted from the thermal simulations (section 2) at the nodal locations along path a-b, as shown on the right of the same figure. A Flir model E60 0.10 hand-held thermal camera was used throughout testing to evaluate the external tread and sidewall temperature distributions.

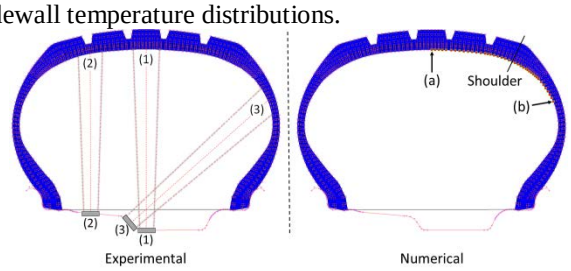

Figure 14: Internal cavity IR measurement locations (left) and thermal simulation model nodal locations along path a-b (right).

4.1 Structural deformation response

The structural deformation of the numerical tire models was validated against experimentally observed responses of an actual tire using the experimental tire test bench. A stereoscopic digital image correlation apparatus was used to analyse the out-of-plane sidewall deformation at the location of maximum radial tread deformation due to contact with the rolling road surface, as illustrated in figure 15. The analysis was performed for a variation in load and inflation pressure, evaluating both the cross sectional sidewall profile shapes and maximum changes in out-of-plane deformation against results obtained from the loading analysis simulations.

Table 6 provides a summary of the maximum out-of-plane sidewall deformation results, including the relative numerical prediction error percentages. The maximum observed prediction error was approximately 11%. A comparison of the numerical and experimental cross sectional sidewall profile shapes is illustrated in Figure 16 for a representative load case. Deflection of the sidewall is proportional to the applied load, and inversely to the internal inflation pressure, with the lowest inflation pressures

resulting in largest deformations. Although there were some variations from the experimental deformations, the overall trend was matched to a sufficient degree for the overall goal, being the prediction of the rate of hysteresis heating owing to deformation, to be achieved.

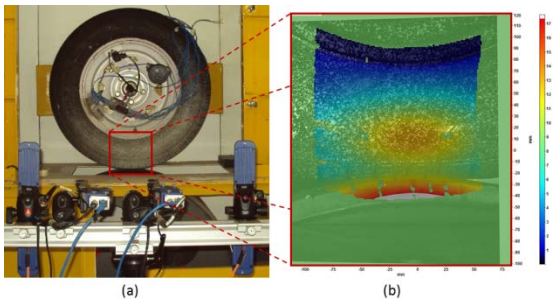

Figure 15: Experimental setup (a) used for sidewall profile measurements. It illustrates the DIC region of interest (red square), along with typical out-of-plane deformation results (b) in mm obtained during post-processing.

Table 6: Maximum out-of-plane sidewall deformations due to radial tread load application as measured by DIC (mm), including relative simulation prediction error percentages.

	100 kPa	
Load	DIC	Prediction error
300 kg	10.7 mm	6.4 %
500 kg	17.4 mm	10.9 %
	175 kPa	
Load	DIC	Prediction error
300 kg	6.4 mm	3.2 %
500 kg	11.7 mm	3.4 %
700 kg	15.6 mm	3.8 %
	250 kPa	
Load	DIC	Prediction error
300 kg	4.5 mm	2.2 %
500 kg	8.1 mm	3.7 %
700 kg	11.8 mm	0.8 %

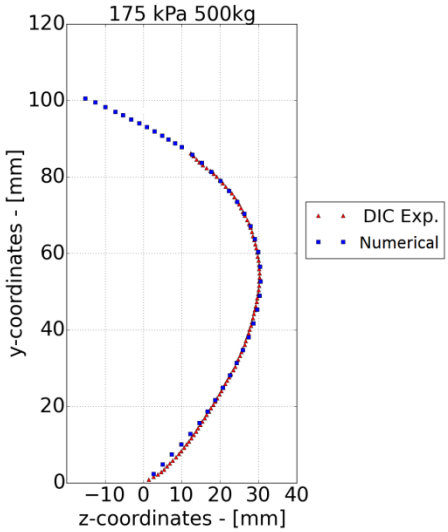

Figure 16: Cross sectional deformed sidewall profiles for a load of 500 kg and inflation pressure of 175 kPa.

The contact pressure distribution profile between the tire tread and rolling road surface was analysed experimentally by means of a Tekscan 5151 N pressure mapping system, comprising of a thin flexible sheet with multiple sensels arranged in square grid. Figure 17 shows the results obtained from experimentation and the simulation models for a representative load case. The simulation model provided a suitable representation of both the experimental distribution profile and maximum observed pressure values.

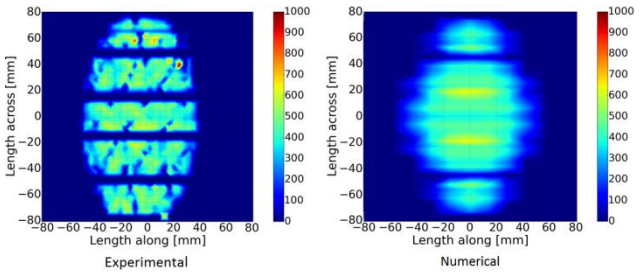

Figure 17: Tread contact pressure (kPa) distribution profiles for a load of 300 kg and inflation pressure of 175 kPa.

4.2 Thermal comparison

An evaluation of the cross sectional equivalent of total strain distributions within the tire region under maximum radial deformation, as obtained from the loading analysis simulations, yielded promising results. As shown in Figure 18 for a load of 700 kg and inflation of 250 kPa, the simulation results indicated strain peaks within the tire shoulder region in contact with the rolling surface.

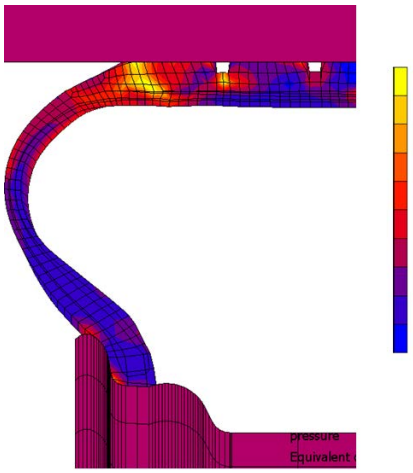

Figure 18: Cross sectional equivalent of total strain distribution simulation result for an inflation of 250 kPa and load of 700 kg.

The elastic strain-energy density obtained from the rolling analysis models (section 2), as used to predict the rate of thermal heat generation due to hysteresis, is a function of the total (principal) strain due to deformation. As a result, the heat generation and steady-state temperature distributions within the tire would be representative of the total strains within its cross section. Figure 19 provides a cross-sectional illustration of the temperature distributions

obtained for a load of 700 kg, inflation of 250 kPa and velocity of 60 km/h.

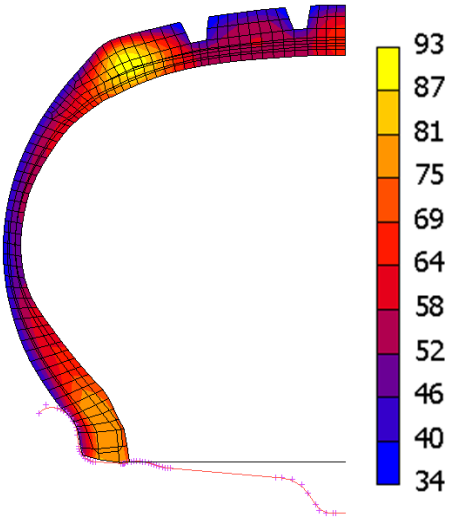

Figure 19: Cross sectional temperature (°C) distribution simulation result for an inflation of 250 kPa, load of 700 kg and rotational velocity of 60 km/h.

The thermal distribution in figure 19 corresponds with the strains of figure 18, with a predicted peak temperature within the tire shoulder region. Additional hot-spots were also present within the central tread and bead regions.

Figure 20 provides an illustration of the internal cavity temperature results along path a-b for the same load case, with reference to figure 14. The area-averaged experimental temperature measurement values are illustrated by straight horizontal green lines, located within the three grey columns. Each column illustrates the measurement region for each of the three IR temperature sensors, with the tire shoulder indicated by the vertical black line. The simulation results indicated temperature peaks within the shoulder and central tread (1) regions, with a relatively cool sidewall, overall similar to the experimental measurements.

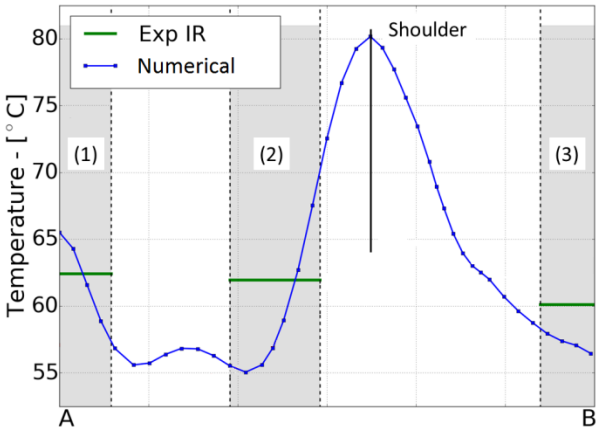

Figure 20: Internal cavity temperature (°C) results comparison for an inflation of 250 kPa, load of 700 kg and rotational velocity of 60 km/h.

Figure 21 provides a comparison of the external tread surface temperature distributions (in °C) for an inflation of 250 kPa, load of 700 kg and rotational velocity of 60 km/h. As with the experimental results, the numerical prediction suggested a peak temperature within the tire shoulder region (1), along with additional temperature hot-spots in the central tread (2) and tread undercut groove (3) regions.

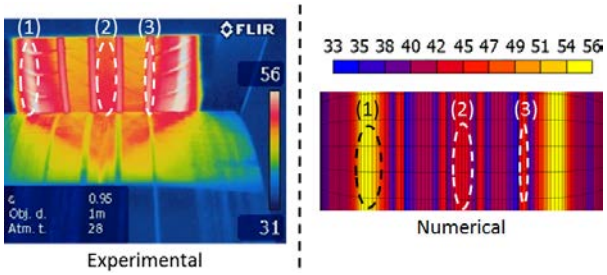

Figure 21: Tread region temperature (°C) comparison for an inflation of 250 kPa, load of 700 kg and rotational velocity of 60 km/h, illustrating the experimental and numerical simulation results.

The results when comparing the sidewall temperature distributions, for the same load case, can be viewed in figure 22, with both the experimental and numerical distributions indicating a peak temperature within the tire shoulder region. This is followed, in both cases, by a cooler central sidewall and finally a slightly warmer bead region.

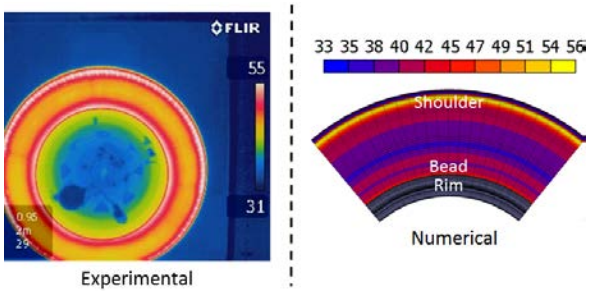

Figure 22: Sidewall region temperature (°C) comparison for an inflation of 250 kPa, load of 700 kg and rotational velocity of 60 km/h, illustrating both experimental and numerical simulation results.

5 Conclusion

A mechanical testing (uni-axial tensile) procedure was performed to identify the material properties of a 215/70R15 steel-belted radial tubeless automobile tire for use in a sequence of finite element thermal simulation models. The tire consisted primarily of three individual rubber regions, with varying degrees of material stiffness, along with internal cord- and steel rebar reinforcements. The stress-strain tensile response of each material was used to identify its structural properties through a sequence of direct curve fits and iterative procedures.

Two- and three-term variants of the Mooney-Rivlin strain-energy based elastomer model were used to represent the rubber materials. Isotropic material definitions were used to represent the structural rebar reinforcements. The stress-strain response curves of combined material tensile test simulation models were good representations of experimental test data when using the identified material properties. Results obtained from a dynamic mechanical analysis of the tire rubber materials were used to determine

http://dx.doi.org/10.17159/2309-8988/2019/v35a3

their hysteresis coefficient values, with results that contradicted the suggestions of published literature.

Numerical distribution trends of the external tread and sidewall surface temperatures corresponded well with experimental results, with maximum values located within the shoulder, circumferential grooves and bead regions. This corresponded to the numerical principal strain distributions under load and experimental internal cavity temperatures. The central tread and central sidewall regions had relatively cool operating temperatures in both cases. In addition, the simulation models provided acceptable predictions of measured tire structural deformation responses.

References

[1] P. I. Dolez, C. Nohile, T. Ha Anh, T. Vu-Khanh, R. Benoît and O. Bellavigna-Ladoux. Exploring the chemical aspects of truck tire blowouts and explosions. *Safety Science*, 46(9): 1334-1344, 2008.

[2] D. Y. Leung and C. L. Wang, Kinetic modeling of scrap tire pyrolysis. *Energy & Fuels*. 13(2):421-427, 1999.

[3] J. R. Cho, H. W. Lee, W. B. Jeong, K. M. Jeong and K. W. Kim. Numerical estimation of rolling resistance and temperature distribution of 3-D periodic patterned tire. *International Journal of Solids and Structures*, 50(1):86-96, 2013.

[4] J. Mc Allen, A. M. Cuitifio and V. Sernas, Numerical investigation of the deformation characteristics and heat generation in pneumatic aircraft tires Part II: Thermal modelling. *Finite Elements in Analysis and Design*. 23(2-4):265-290, 1996.

[5] T. Tang, D. Johnson, R. E. Smith and S. D. Felicelli. Numerical evaluation of the temperature field of steady-state rolling tires. *Applied Mathematical Modelling*, 38(5-6):1622-1637, 2014.

[6] S. Ghosh. *Investigation on Role of Fillers on Viscoelastic Properties of Tire Tread Compounds*. PhD Thesis, Maharaja Sayajirao University of Baroda, India, 2011.

[7] H. S. Yin, Y. S. Hu, H. Zhang, M. M. Yang and Y. T. Wei. Truck tire thermal-mechanical FEA and DMA with application to endurance evaluation. *Tire Science and Technology*, 34(4):220-236.

[8] R. Brancati, S. Strano and F. Timpone. An analytical model of dissipated viscous and hysteretic energy due to interaction forces in a pneumatic tire: Theory and experiments. *Mechanical Systems and Signal Processing*, 25(7):2785-2795, 2011.

[9] K. Ivan and K. Jan. FE analysis of automobile tire. In *Proceedings of Advanced Research in Scientific Areas*, December, 2012.

[10] W. B. Blommestein. *Experimentally Determined Material Parameters for Temperature Prediction of an Automobile Tire using Finite Element Analysis*. MEng Thesis, Stellenbosch University, South Africa, 2016.

[11] M.H.R. Ghoreishy, M. Malekzadeh and H. Rahimi. A parametric study on the steady state rolling behaviour of a steel-belted radial tyre. *Iranian Polymer Journal*. 16(8):539-548, 2007.

[12] N. Korunović, M. Trajanović and M. Stojković. FEA of tyres subjected to static loading. *Journal of the Serbian Society for Computational Mechanics*, 1(1):87-98, 2007.

[13] N. Korunović, M. Trajanović, M. Stojković, D. Mišić and J. Milovanović. Finite Element Analysis of a Tire Steady Rolling on the Drum and Comparison with Experiment. *Strojniški vestnik - Journal of Mechanical Engineering*, 57(12):888-897, 2011.

[14] J. Marais. *Numerical Modelling and Evaluation of the Temperature Distribution in an Earthmover Tyre: Establishing a Safe Operating Envelope*. MEng Thesis, Stellenbosch University, South Africa, 2017.

[15] H. Hölscher, M. Tewes, N. Botkin, M. Löhndorf, K.H. Hoffmann, and E. Quandt. Modeling of pneumatic tires by a finite element model for the development a tire friction remote sensor. Unpublished paper, Center of Advanced European Studies and Research, 2004.

[16] X. Yang, O. A. Olatunbosun and E. O. Bolarinwa. Materials resting for finite element tire model. *SAE International Journal of Materials and Manufacturing*, 3(1):211-220, 2010.

[17] J. C. Maritz. *Numerical Modelling and Experimental Measurement of the Temperature Distribution in a Rolling Tire*. MEng Thesis, Stellenbosch University, South Africa, 2015.

[18] Y. J. Lin and S. J. Hwang. Temperature prediction of rolling tires by computer simulation. *Mathematics and Computers in Simulation*, 67(3):235-249, 2004.

[19] A. N. Gent. *Engineering with Rubber: How to Design Rubber Components*. Hanser Publishers, Munich, 3rd edition, 2012.

[20] S. Chae. *Nonlinear Finite Element Modeling and Analysis of a Truck Tire*. PhD Thesis, Pennsylvania State University, USA, 2006.

[21] A. L. Browne and L. E. Wickliffe. Convective Heat Transfer Coefficients at the Tire Surface: A Parametric Study. General Motors Research Publications, 1980.

[22] T. G. Ebbot, R. L. Hohman, J. P. Jeusette and V. Kerchman. Tire temperature and rolling resistance prediction with finite element analysis. *Tire Science and Technology*, 27(1):2-21, 1999.

[23] M. C. Assaad, B. Kimble, Y. M. Huang, R. Burgan, G. C. Fralick, J. D. Wrbanek and J. M. Gonzalez. Thin film heat flux sensor for measuring film coefficient of rubber components of a rolling tire. *Tire Science and Technology*, 36(4):275-289, 2008.

[24] Y. A. Cengel and A. J. Ghajar. *Heat and Mass Transfer: Fundamentals and Applications*. McGraw-Hill, New-York, 5th edition, 2015.

[25] M. C. Boyce and E. M. Arruda. Constitutive models of rubber elasticity: A review. *Rubber Chemistry and Technology*, 73(3):504-523, 2000.

[26] N. Kumar and V. V. Rao. Hyperelastic Mooney-Rivlin Model: Determination and physical interpretation of

material constants. *MIT International Journal of Mechanical Engineering*, 6(1):43-46, 2016.

[27] MSC. Basic Nonlinear Analysis using Marc and Mentat: MAR101 Course Notes. Santa, 2013.

[28] VR&D. DOT User's manual. Colorado Springs, USA, 2001.